Journal of Cerebral Blood Flow & Metabolism (2011) 31, 2169–2180

www.jcbfm.com

In vivo variation in metabotropic glutamate receptor subtype 5 binding using positron emission tomography and [^{11}C]ABP688

Christine DeLorenzo[1], JS Dileep Kumar[1,2,3], J John Mann[1,2,3] and Ramin V Parsey[1,2]

[1]*Division of Molecular Imaging and Neuropathology, Department of Psychiatry, Columbia University, New York, New York, USA;* [2]*New York State Psychiatric Institute, New York, New York, USA;* [3]*Department of Radiology, Columbia University, New York, New York, USA*

The metabotropic glutamate receptor subtype 5 (mGluR5) has been implicated in the pathophysiology of mood and anxiety disorders. Recently, a positron emission tomography (PET) tracer exhibiting high selectivity and specificity for mGluR5, 3-(6-methyl-pyridin-2-ylethynyl)-cyclohex-2-enone-*O*-^{11}C-methyl-oxime ([^{11}C]ABP688), was developed. In this work, eight healthy adult male humans were imaged twice to assess within-subject [^{11}C]ABP688 binding variability using PET. In seven of the eight subjects, significantly higher binding was observed during the second (retest) scan. This binding increase could not be definitively explained by differences in ligand injected mass or dose, or changes in metabolism between scans. In addition, this type of systematic binding increase was not observed in a [^{11}C]ABP688 test–retest study performed by our group on anaesthetized baboons. It is therefore possible that the increased binding was because of physiological changes occurring between scans, such as changes in endogenous glutamate levels. If PET imaging with [^{11}C]ABP688 could detect such differences, as preliminary evidence suggests, it could be used to help uncover the role of glutamate in the pathophysiology of brain disorders. However, regardless of its ability to detect endogenous glutamate differences, [^{11}C]ABP688 binding variability could make accurate assessments of drug occupancy or group differences using this ligand difficult.
Journal of Cerebral Blood Flow & Metabolism (2011) **31,** 2169–2180; doi:10.1038/jcbfm.2011.105; published online 27 July 2011

Keywords: brain imaging; glutamate; molecular imaging; neurotransmitters; positron emission tomography

Introduction

Glutamate is the primary neurotransmitter in the brain, found in as many as 90% of brain neurons, with 80% to 90% of synapses being glutamatergic (Siegel, 2006). Perhaps because of its universality, initial investigations of the neurobiology of mood disorders focused on monoamine dysfunction. Increasingly, however, diverse studies have implicated glutamatergic, in addition to monoaminergic, pathway dysfunction in the pathophysiology of mood disorders (Kendell *et al*, 2005). It is now believed that the availability of glutamate in the brain contributes to its impact in a spectrum of neurological and psychiatric disorders (Kendell *et al*, 2005). As an example of this, biochemical and electrophysiological studies have shown that glutamate receptors are influenced by traditional antidepressant treatments, which primarily target monoaminergic transmission (Pilc *et al*, 2008). Because of their important role in brain function, elucidating the mechanism of action of glutamate receptors would clarify glutamate's role in physiological and pathological conditions.

There are two main types of glutamate receptors—ionotropic, responsible for fast excitatory transmission, and metabotropic (mGlu), which exert a modulatory role on the central nervous system (Palucha and Pilc, 2007). One mGlu receptors in particular, the mGlu receptor subtype 5 (mGluR5), has been localized in moderate to high levels in brain regions associated with depression (Spooren *et al*, 2003). Antagonists of mGluR5 have potential as effective antidepressants (Palucha and Pilc, 2007). In addition, mGluR5 may be a therapeutic target for schizophrenia (Lindsley *et al*, 2006; Liu *et al*, 2008), psychostimulant addiction (Gass *et al*, 2009; Markou, 2009), Parkinson's disease (Aguirre *et al*, 2005; Turle-Lorenzo *et al*, 2005), attention-deficit and

Correspondence: Dr C DeLorenzo, New York State Psychiatric Institute, Unit 42, 1051 Riverside Drive, New York, NY, 10032, USA.
E-mail: cd2415@columbia.edu
Sources of Support: Eli Lilly and Company
Received 7 February 2011; revised 5 June 2011; accepted 14 June 2011; published online 27 July 2011

hyperactivity disorder (Elia *et al*, 2010), as well as fragile X syndrome, the most common inherited form of mental retardation and autism (Dolen and Bear, 2008).

Although the importance of mGluR5 has been established, its role in the pathophysiology of disease and its effectiveness as a therapeutic target is difficult to assess without the ability to measure mGluR5 expression or mGluR5 antagonist occupancy. To this end, 3-(6-methyl-pyridin-2-ylethynyl)-cyclohex-2-enone-*O*-^{11}C-methyl-oxime ([^{11}C]ABP688), a highly selective allosteric antagonist of mGluR5 *in vitro* with high selectivity for mGluR5 *in vivo*, has been developed for use in humans (Ametamey *et al*, 2006). The use of this compound as a positron emission tomography (PET) tracer provides the ability to visualize and study mGluR5 binding and distribution *in vivo*. In two human studies, this PET ligand was shown to have the highest uptake in mGluR5-rich regions and to have favorable kinetics (Ametamey *et al*, 2007; Treyer *et al*, 2007).

Although interindividual variance of [^{11}C]ABP688 binding has been evaluated using PET, the only way to assess intraindividual binding variation is by performing repeated [^{11}C]ABP688 scans on the same subject. One such study was recently performed by our group on anesthetized *Papio anubis*. In that study, [^{11}C]ABP688 test–retest volume of distribution was found to be remarkably stable, with the average percent difference varying between 4.3% and 8.2% across all brain regions (DeLorenzo *et al*, 2011). To determine whether this binding consistency remains in awake humans, in this study, [^{11}C]ABP688 binding in eight healthy adult male humans was assessed using a test–retest paradigm.

Materials and methods

Subjects

Eight healthy men between the ages of 19 and 34 years completed this study (mean age: 25.4 ± 5.8 years). Three subjects (37.5%) reported their race as Hispanic, three (37.5%) as black, one (12.5%) as Asian, and one (12.5%) as white (non-Hispanic). Inclusion criteria were assessed by the following: history, Structured Clinical Interview for the Diagnostic and Statistical Manual of Mental Disorders (SCID), review of systems, physical examination, routine blood tests, urine toxicology, and electrocardiography. The inclusion criteria consisted of: (1) men between the ages of 18 and 65 years and (2) capacity to provide written informed consent. Exclusion criteria included: (1) lifetime history of alcohol or substance abuse or dependence, (2) an Axis I or Axis II Cluster B disorder diagnosis, as assessed by the SCID, (3) presence and/or history of a clinically significant major neurological or psychiatric disorder, (4) presence and/or history of first-degree relative with history of major depression, schizophrenia, schizoaffective disorder, or suicide attempt, (5) presence and/or history of two or more first-degree relatives with a history of substance dependence, (6) laboratory tests with clinically significant abnormalities or positive urine toxicology screen, (7) evidence of human immunodeficiency virus, (8) history of head trauma with prolonged loss of consciousness (>10 minutes), any neurological condition including stroke or seizure (excluding a single childhood febrile seizure), or a history of migraine headaches, (9) history of adverse drug reactions or intolerance to more than three types of systemically administered medications, (10) use of any prescription or over-the-counter medication (including herbal remedies or diet aids) within 14 days of the imaging session (multivitamins are permitted), or (11) subject is a Lilly employee. The Institutional Review Boards of Columbia University Medical Center and the New York State Psychiatric Institute approved the protocol. Subjects gave written informed consent after receiving an explanation of the study.

Radiochemistry

Radiosynthesis of [^{11}C]ABP688 was achieved using the procedure outlined by Ametamey *et al* (2006), with slight modification. [^{11}C]MeOTf was trapped into an acetone (400 mL) solution containing 0.5 mg of desmethyl-ABP688 and 10 μL NaOH (5 N) at room temperature for 5 minutes. The crude product was loaded into a semipreparative high performance liquid chromatography (HPLC) column (Phenomenex C18, Phenomenex, Torrance, CA, USA), eluted with 50:50 (acetonitrile/0.1 mol/L AMF, 10 mL/min), and the product fraction (major diastereomer) was collected between 9 and 10 minutes based on a γ-detector. The collected fraction was then diluted with deionized water (100 mL), passed through a C-18 SepPak (Waters, Milford, MA, USA), and washed with water (2×20 mL). After the water rinse, the product was eluted from the SepPak with 1 mL of ethanol. A small portion of the product was analyzed with analytical HPLC for chemical and radiochemical purities, specific activity, and other quality control indices. The remaining ethanol solution was diluted with 9 mL of normal saline, filtered through a 0.22-μm filter, and used for further studies. The total time required for the synthesis of [^{11}C]ABP688 was 30 minutes from the end of bombardment.

Positron Emission Tomography

All subjects underwent two identical PET scans, test and retest, on the same day, separated by an $\sim$2-hour break. The one exception was subject no. 4 who, because of scheduling constraints, underwent PET imaging on two consecutive days. PET imaging was performed with an ECAT EXACT HR+ (Siemens/CTI, Knoxville, TN, USA), with 63 slices covering an axial field of view of 15.5 cm and axial sampling of 2.425 mm, in 3D mode. A 10-minute transmission scan was acquired before injection. At the end of the transmission scan, [^{11}C]ABP688 was administered intravenously as a bolus over 30 seconds. After injection of [^{11}C]ABP688, emission data were collected for 60 minutes in listmode. The listmode data were then binned into 20 frames (10 at 1 minute duration and 10 at 5 minute duration). Images were reconstructed using

attenuation correction from the transmission data, as previously described (DeLorenzo *et al*, 2009*b*).

Magnetic Resonance Imaging

Magnetic resonance images (MRIs) were acquired on a 3-T Signa Advantage system (GE Healthcare, Waukesha, WI, USA), as previously described (Ogden *et al*, 2007). The final voxel size was $1.02 \times 1.02 \times 1.00$ mm, with an acquisition time of 11 minutes.

Input Function Measurement

Before PET imaging, catheters were inserted in the radial artery and forearm veins for arterial blood sampling and radioisotope injection, respectively. Arterial samples were collected automatically every 10 seconds for the first 2 minutes, followed by every 20 seconds until minute four, then manually at 5, 8, 10, 15, 20, 30, 40, 50, and 60 minutes, for a total of 27 samples. Radioactivity of 200 μL aliquots of centrifuged plasma samples was measured in a 1480 Wizard 3 M automatic γ counter (Wallac, Turku, Finland).

Free fraction measurements were performed using an ultrafiltration technique as previously described (Ogden *et al*, 2007). However, these measurements yielded inconsistent results, preventing accurate free fraction determination. A SepPak assay of five of the arterial blood samples (at 2, 5, 15, 30, and 60 minutes) was used to establish unmetabolized parent compound levels. To perform this assay, 200 μL of plasma was pipetted into 2.5 mL of deionized water in a polypropylene tube. The mixture was vortexed for 10 seconds and the diluted plasma was loaded onto a SepPak tC18 cartridge (6 cc/1 gm; 37 to 55 μm; Waters). The SepPak was eluted dropwise with 5 mL of water and the leftover parent and metabolite (in the combined eluted solution) activity were measured.

Unmetabolized parent fraction levels were fit with a Hill function (Wu *et al*, 2007). The input function was calculated as the product of the interpolated parent fraction and the total plasma counts. These combined data were then fit as the combination of a straight line and the sum of three exponentials, describing the function before and after the peak, respectively.

Image Analysis

All images were analyzed using MATLAB (MathWorks, Natick, MA, USA). The last 13 frames of an individual PET study were registered to the eighth frame using the FMRIB linear image registration tool (FLIRT), version 5.0 (FMRIB Image Analysis Group, Oxford, UK), to correct for subject motion during the scan. Automatic regions of interest were obtained using nonlinear registration techniques to warp 18 manually outlined MRIs to the target image. A total of 34 regions were previously manually traced by experienced technicians on the 18 MRIs, as previously described (Ogden *et al*, 2007). Before applying the 18 templates to the target images, each target subject's MRI was first preprocessed with SPM5 for segmentation into gray matter, white matter, and CSF (Wellcome Trust Centre for Neuroimaging, London, UK), and with an automated skull-stripping algorithm (atropos; Avants *et al*, 2010). Each of the 18 templates was registered to the target brain MRI using the Automatic Registration Toolbox (ART; Ardekani *et al*, 2005), which was a top performer in an evaluation of 14 nonlinear brain registration algorithms (Klein *et al*, 2009). The regional label for each target voxel was then determined by evaluating the percentage of the 18 normalized brains that were labeled as that region. The labels are therefore probabilistic and these probabilities are used in the calculation of the time–activity curves (TACs).

The mean PET image was coregistered to the subject's MRI to apply regions of interest to the mean PET image, and individual PET frames. PET-to-MRI transformations were computed using FLIRT with a mutual information cost function, six degrees of freedom, and trilinear interpolation. Eight different coregistration possibilities with varying source/target images and weighting masks were performed, as previously described (DeLorenzo *et al*, 2009*a*). The optimum transformation was chosen as the one that maximized a mutual information cost function and verified by visual inspection. Time–activity curves were generated by plotting the measured activity within a region over the time course of the PET acquisition.

Outcome Measure Calculation

The outcome measure closest to the receptor density is BP_F (B_{avail}/K_D), where B_{avail} is the density of available receptors and K_D is the equilibrium dissociation constant (Innis *et al*, 2007). As the determination of BP_F requires accurate measurement of the free fraction (f_p) and [^{11}C]ABP688 free fraction measurements were unreliable, BP_F estimations were unreliable. Therefore, in this work, the measurement closest to receptor density, while maintaining reliability, was $BP_P f_p B_{avail}/K_D$. BP_P can be calculated as $V_T - V_{ND}$, where V_T is the volume of distribution (ratio of the concentration of the ligand in the region to that in the plasma at equilibrium) and V_{ND} is the volume of distribution of the reference region, representing the non-displaceable V_T (Innis *et al*, 2007). The reference region used in this work was cerebellar gray matter, which was found to be the most suitable reference region for this ligand (DeLorenzo *et al*, 2011). Although BP_P is the outcome measure of choice when the free fraction is not measured, the advantage of using V_T as an outcome measure is that it is not influenced by estimations of V_{ND}.

In addition to V_T and BP_P, the outcome measure BP_{ND} ($(V_T - V_{ND})/V_{ND}$) was calculated (Innis *et al*, 2007). As BP_{ND} represents the concentration of ligand in the region of interest relative to the reference region, it is insensitive to arterial input function quantification and can therefore provide another important measure by which to evaluate ABP688 binding.

For regional analysis, outcome measures were calculated using an unconstrained two-tissue compartment (2TC) model. According to previous human studies (Treyer *et al*, 2007), 2TC models are superior to one-tissue compartment models for modeling [^{11}C]ABP688 tracer kinetics. In addition, the test–retest experiments performed in non-human primates indicated that the unconstrained 2TC model optimally fit [^{11}C]ABP688 TACs

(DeLorenzo *et al*, 2011). Because of the computational expense of the 2TC method, the Logan graphical approach (Logan *et al*, 1990), which results in outcome measures highly correlated to those found by the 2TC (Treyer *et al*, 2007), was used for voxel analysis.

Statistical Analysis

To determine the significance of detected differences in test–retest outcome measures, a linear mixed effects model with region as a fixed effect (for all regions listed in Table 1) and subject and scan (nested within subject) as random effects was applied to the data. Subsequently, *post hoc* analysis was performed on the outcome measures from each region individually using a two-tailed, paired *t*-test. In both cases, significance level was defined as 0.05.

To compare within-subject to between-subject variability, the intraclass correlation coefficient (ICC) was calculated (Shrout and Fleiss, 1979). This measure varies between −1 (indicating low reliability) and 1 (indicating maximum reliability).

Results

Regional Uptake

The uptake of [^{11}C]ABP688 appears greater in regions of the brain with known distributions of mGluR5, such as the insula, ventral striatum, temporal lobe, cingulate, and medial prefrontal cortex. Lower binding is observed in the thalamus and cerebellum.

To visualize this binding pattern clearly, an aggregate image was created of all subjects (Figure 1). To create this aggregate image, V_T was calculated at every PET image voxel for every subject and each voxel map was then aligned to the subject's MRI using the calculated coregistration transform (see Materials and methods—Image Analysis). The subject's MRI was then nonlinearly warped to a high-resolution template (Holmes *et al*, 1998) using ART, and the resulting nonlinear transform was used to bring each subject's V_T voxel map into the space of the high-resolution template.

Time–Activity Curve Fits

Examples of the unconstrained 2TC modeling method fits for high-, medium-, and low-binding regions are shown in Figure 2.

Test–Retest Results

Figure 3 shows the test–retest effect on the outcome measures V_T and BP_{ND}. As evident from the graphs, an increase in binding (on retest) was observed across most regions and subjects. Applying the linear mixed effects model to the V_T data (Figure 3, top) revealed a significant test–retest effect across all regions ($P = 0.01$). When this linear mixed effects model was applied to the BP_{ND} data (Figure 3, bottom) for all regions except the reference region (where BP_{ND} cannot be calculated), a significant test–retest effect across all regions was also observed ($P = 0.05$). For completeness, the linear mixed effects model was also applied to the BP_P data, and results were similar ($P = 0.01$).

Table 1 shows the mean V_T, BP_P, and BP_{ND} values across all subjects, and the average percent difference between these values. It also lists both the *P* values associated with the regional *post hoc* analysis and ICC values within each region. The *post hoc* testing indicates that, for most regions, the test–retest difference is either significant or at trend level. The highest ICC value (0.76) was that of the reference region V_T. Aside from that region, the range of ICCs was 0.39 to 0.73 (V_T), 0.15 to 0.73 (BP_P), and 0.14 to 0.70 (BP_P). Within each region, V_T ICC values were, in general, higher than BP_P ICC values, and BP_{ND} ICC values were the lowest.

Although the unconstrained 2TC model fit the TACs well, in light of the observed unexpected increase in binding between test and retest, the data were modeled using four additional techniques: (1) a 2TC model constrained such that the ratio of kinetic constants, K_1/k_2, for each region is restricted to the ratio of K_1 to k_2 in the reference region (Parsey *et al*, 2000b), (2) a 2TC model fit using non-iterative methods in which the experimental data are matched to the most similar curve in a library of precalculated functions, rather than by performing a nonlinear least squares iterative fit, (3) Logan graphical analysis, in which outcome measures are calculated from the slope of the linear part of an integral plot (Logan *et al*, 1996), and (4) likelihood estimation in graphical analysis, which has been shown to reduce bias introduced by the Logan approach (Ogden, 2003). One-tissue compartment models were not used in the comparison because they did not fit the data well (data not shown). For all four models tested, the results were similar to those found using an unconstrained iterative 2TC method. That is, regardless of the chosen model, V_T within each region of interest increased between test and retest by 11% to 21% on average (Table 2).

Potential Causes of Observed Results

It is possible that the observed increases in binding could be because of differences in injected mass or dose of the ligand between test and retest scans. However, no significant correlation was found between injected mass and the V_T of any region. For the non-reference regions listed in Table 1, the correlations between injected mass and regional V_T varied between −0.27 and −0.10 (*P* values: 0.30 to 0.71). The correlation between injected mass and V_T of the reference region was −0.48 ($P = 0.06$). In addition, even if a correlation between injected

Table 1 Volume of distribution (V_T, mL/cc), and two measures of binding potential (BP_P, mL/cc, and BP_{ND}, unitless) for test and retest scans

	Test	*Retest*	*Percent difference (%)*	P *value*	*ICC*
Insula					
V_T	2.29 ± 0.55	2.69 ± 0.51	19.7 ± 13.7	0.02	0.55
BP_P	1.06 ± 0.38	1.36 ± 0.27	31.3 ± 21.0	0.02	0.40
BP_{ND}	0.87 ± 0.28	1.03 ± 0.15	22.9 ± 22.5	0.08	0.37
Ventral striatum					
V_T	2.22 ± 0.54	2.60 ± 0.42	20.0 ± 17.1	0.05	0.40
BP_P	0.99 ± 0.40	1.27 ± 0.18	35.4 ± 26.0	0.07	0.15
BP_{ND}	0.82 ± 0.30	0.97 ± 0.18	31.4 ± 21.9	0.17	0.25
Temporal lobe					
V_T	2.09 ± 0.57	2.53 ± 0.54	20.7 ± 17.1	0.01	0.55
BP_P	0.86 ± 0.38	1.20 ± 0.31	36.8 ± 28.8	0.01	0.41
BP_{ND}	0.70 ± 0.26	0.90 ± 0.19	30.5 ± 27.6	0.04	0.30
Cingulate					
V_T	2.09 ± 0.56	2.45 ± 0.52	19.1 ± 17.2	0.04	0.57
BP_P	0.86 ± 0.34	1.12 ± 0.28	32.1 ± 29.1	0.04	0.38
BP_{ND}	0.70 ± 0.22	0.85 ± 0.17	24.4 ± 28.6	0.11	0.19
Medial prefrontal cortex					
V_T	2.07 ± 0.51	2.43 ± 0.51	18.9 ± 13.4	0.02	0.61
BP_P	0.84 ± 0.31	1.10 ± 0.25	34.1 ± 21.7	0.02	0.41
BP_{ND}	0.69 ± 0.21	0.83 ± 0.11	26.8 ± 24.1	0.09	0.14
Dorsal putamen					
V_T	2.06 ± 0.47	2.36 ± 0.44	17.0 ± 14.1	0.05	0.57
BP_P	0.83 ± 0.28	1.02 ± 0.20	29.0 ± 20.3	0.06	0.36
BP_{ND}	0.68 ± 0.20	0.78 ± 0.14	23.2 ± 18.9	0.20	0.36
Entorhinal cortex					
V_T	2.03 ± 0.52	2.39 ± 0.51	17.3 ± 16.6	0.02	0.60
BP_P	0.80 ± 0.36	1.06 ± 0.32	32.0 ± 26.0	0.01	0.60
BP_{ND}	0.66 ± 0.26	0.81 ± 0.23	25.8 ± 24.1	0.04	0.63
Posterior parahippocampal gyrus					
V_T	2.00 ± 0.40	2.34 ± 0.47	19.7 ± 14.3	0.05	0.39
BP_P	0.77 ± 0.24	1.00 ± 0.24	34.9 ± 22.9	0.04	0.17
BP_{ND}	0.64 ± 0.20	0.76 ± 0.18	25.4 ± 20.8	0.11	0.44
Parietal lobe					
V_T	1.93 ± 0.48	2.30 ± 0.48	18.9 ± 13.7	0.01	0.62
BP_P	0.70 ± 0.29	0.97 ± 0.25	34.5 ± 22.9	< 0.01	0.48
BP_{ND}	0.57 ± 0.19	0.73 ± 0.14	27.6 ± 23.5	0.02	0.30
Orbital prefrontal cortex					
V_T	1.91 ± 0.52	2.29 ± 0.49	19.7 ± 14.3	0.01	0.64
BP_P	0.68 ± 0.33	0.96 ± 0.27	38.9 ± 35.1	0.01	0.45
BP_{ND}	0.55 ± 0.22	0.73 ± 0.16	36.6 ± 34.8	0.06	0.18
Dorsolateral prefrontal cortex					
V_T	1.92 ± 0.50	2.28 ± 0.51	18.6 ± 13.6	0.01	0.65
BP_P	0.70 ± 0.29	0.94 ± 0.27	34.0 ± 25.6	0.01	0.53
BP_{ND}	0.56 ± 0.19	0.71 ± 0.14	25.6 ± 28.5	0.04	0.34
Amygdala					
V_T	1.95 ± 0.43	2.21 ± 0.45	14.8 ± 9.1	0.02	0.73
BP_P	0.72 ± 0.31	0.88 ± 0.25	27.9 ± 20.5	0.03	0.73
BP_{ND}	0.60 ± 0.25	0.67 ± 0.18	24.8 ± 25.9	0.30	0.70
Dorsal caudate					
V_T	1.82 ± 0.48	2.20 ± 0.49	22.1 ± 12.9	0.01	0.59
BP_P	0.59 ± 0.32	0.87 ± 0.26	49.3 ± 33.9	< 0.01	0.49
BP_{ND}	0.48 ± 0.24	0.65 ± 0.13	39.3 ± 39.6	0.02	0.42
Occipital lobe					
V_T	1.84 ± 0.47	2.16 ± 0.45	16.9 ± 13.5	0.01	0.68
BP_P	0.61 ± 0.27	0.82 ± 0.21	34.3 ± 21.7	< 0.01	0.56
BP_{ND}	0.49 ± 0.17	0.62 ± 0.12	29.4 ± 21.6	0.03	0.32

Table 1 *Continued*

	Test	*Retest*	*Percent difference (%)*	P *value*	*ICC*
Hippocampus					
V_T	1.81 ± 0.52	2.14 ± 0.48	18.4 ± 16.9	0.01	0.68
BP_P	0.58 ± 0.33	0.81 ± 0.27	44.0 ± 39.4	0.01	0.59
BP_{ND}	0.46 ± 0.24	0.61 ± 0.18	39.8 ± 39.5	0.07	0.43
Thalamus					
V_T	1.42 ± 0.37	1.66 ± 0.34	17.7 ± 12.5	0.01	0.69
BP_P	0.19 ± 0.17	0.33 ± 0.11	82.6 ± 81.4	< 0.01	0.48
BP_{ND}	0.15 ± 0.13	0.25 ± 0.08	73.4 ± 84.9	0.02	0.38
Cerebellar gray matter					
V_T	1.23 ± 0.28	1.34 ± 0.30	13.5 ± 10.6	0.14	0.76
BP_P	0.00 ± 0.00	0.00 ± 0.00	—	—	—
BP_{ND}	0.00 ± 0.00	0.00 ± 0.00	—	—	—

ICC, intraclass correlation coefficient.
The mean and standard deviation of V_T, BP_P, and BP_{ND} values are shown for all test and retest scans (columns 2 and 3). For each test–retest pair, the percent difference was calculated as the absolute difference between V_T (or BP_P or BP_{ND}) values divided by the mean of the two V_T (or BP_P or BP_{ND}) values. The average of these percent differences over all subjects is indicated (column 4). For most regions, the increase in binding was significant, as indicated by the *P* value of the *post hoc* analysis (two-tailed, paired *t*-test, column 5). ICCs are indicated in the last column. Regions are listed in order from the highest to the lowest mean V_T.

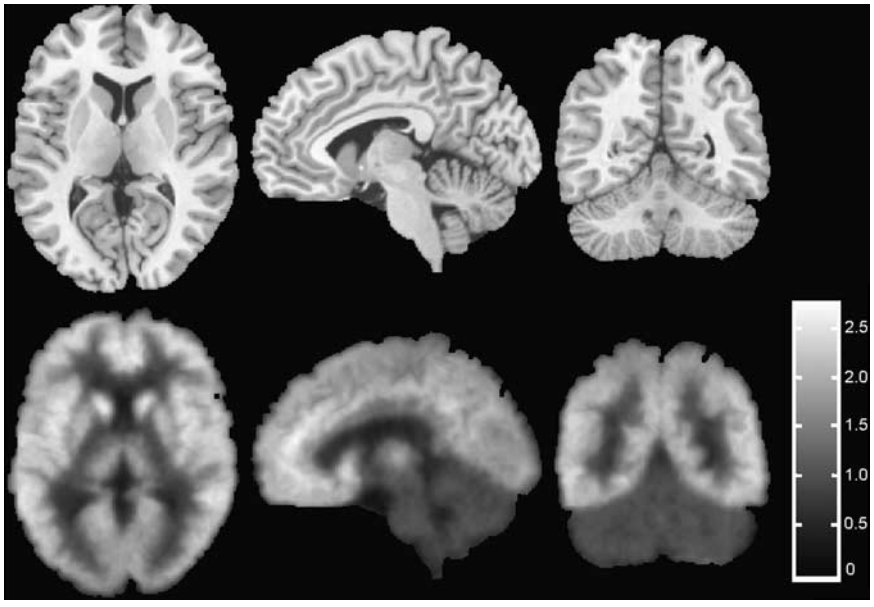

Figure 1 Axial, sagittal, and coronal views of [^{11}C]ABP688 binding. For each positron emission tomography image acquired ($n = 16$), the volume of distribution (V_T) was calculated at every voxel using the Logan graphical approach (Logan *et al*, 1990). The top row shows axial, sagittal, and coronal views of the magnetic resonance image template for anatomical reference. The bottom row shows the corresponding axial, sagittal, and coronal views of the mean [^{11}C]ABP688 V_T image (over all subjects), in the space of the high-resolution template (see text for details). The V_T value associated with each color is indicated by the color bar.

mass and V_T were found, injected masses were comparable across scans (Table 3). Mean injected mass was 4.33 ± 1.73 μg and 4.47 ± 1.09 μg for test and retest scans, respectively ($P = 0.84$). Similarly, no significant differences were found in injected doses or specific activities between test and retest scans. Mean injected dose was 9.79 ± 3.99 mCi and 12.71 ± 3.95 mCi ($P = 0.14$), and mean specific activity was 0.66 ± 0.40 mCi/nmol and 0.76 ± 0.41 mCi/nmol ($P = 0.54$), for test and retest scans, respectively.

As injected masses, doses, and specific activities were similar between scans, subject metabolism changes were investigated. To assess this, each subject's clearance (injected dose divided by the area under the metabolite-corrected plasma curve; Hirvonen *et al*, 2008) was calculated. However, clearance rates did not significantly change between test and

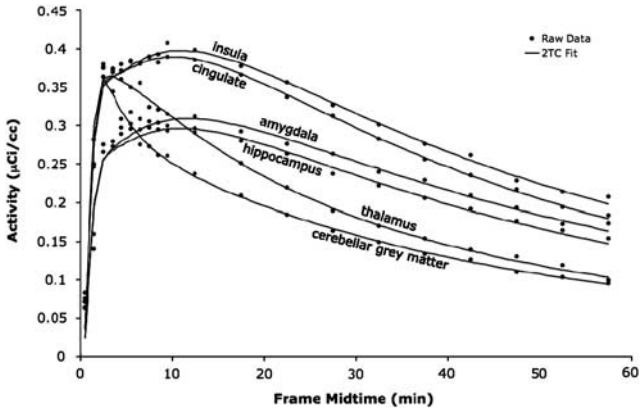

Figure 2 Time–activity curve fits in one subject. The raw data (black circles, mean of the activity within the region) are shown for two regions with high binding (insula and cingulate), two with moderate binding (amygdala and hippocampus), and two with low binding (thalamus and cerebellar gray matter). These raw data were fit with an unconstrained, iterative two-tissue compartment model (2TC, black lines).

retest (Table 3). Average clearance rates were 74.7 ± 8.8 L/h and 81.2 ± 13.0 L/h for test and retest scans, respectively ($P = 0.20$). Although the ICC of clearance was low (0.26), ICCs of area under the percent parent curve (0.77) and the time to peak of the plasma fit (0.74) indicated high reliability.

To illustrate how it is possible that measured binding can increase despite similar input functions, Figure 4 shows an example of a case in which the subject's metabolite and plasma activity curves were almost indistinguishable, yet the time–activity curves for test and retest scans still varied considerably. V_T values estimated from these TACs varied by 19.9% (2.60 mL/cc versus 3.17 mL/cc for test and retest, respectively).

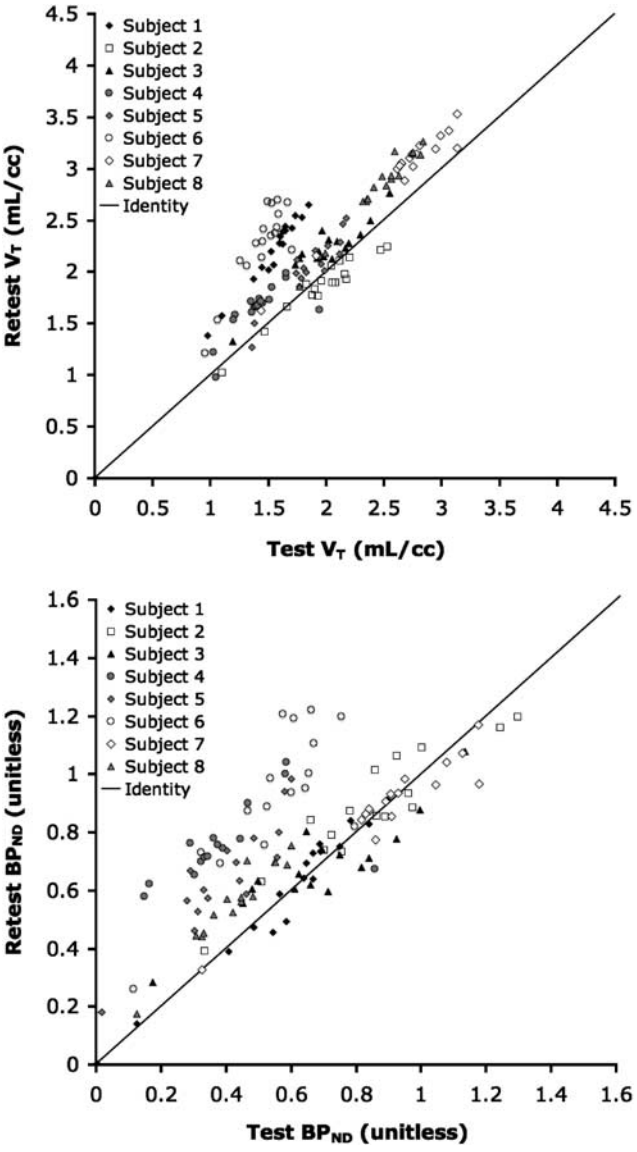

Figure 3 Comparison of volume of distribution (V_T, top) and binding potential (BP_{ND}, bottom) between test and retest. V_T and BP_{ND} were calculated using unconstrained, iterative two-tissue compartment method. In both graphs, the identity line is plotted for reference. In most cases, binding was higher in the retest scans than the test scans.

Discussion

Previous work has shown that the 2TC models fit [^{11}C]ABP688 TACs better than the one-tissue compartment models (Treyer *et al*, 2007), and our test–retest [^{11}C]ABP688 studies in baboons indicated that the optimal model for [^{11}C]ABP688 is the unconstrained 2TC model (DeLorenzo *et al*, 2011). For these reasons, an unconstrained 2TC modeling method was the primary modeling technique used in this work. As Figure 2 indicates, this modeling method fit the data well. However, Table 2 suggests that outcome measure results were not strongly sensitive to model choice.

In previous *in vitro*, rodent, and primate studies, [^{11}C]ABP688 exhibited high specificity and selectivity for mGluR5 (Ametamey *et al*, 2006; DeLorenzo *et al*, 2011; Hintermann *et al*, 2007; Wyss *et al*, 2007). In human studies, this PET ligand was shown to have the highest uptake in mGluR5-rich regions (Ametamey *et al*, 2007) and favorable kinetics (Treyer *et al*, 2007). However, V_T estimates varied considerably between subjects, with coefficients of variation ranging between 16.7% and 32.1% across regions using an unconstrained 2TC model (Treyer *et al*, 2007). Without performing repeated PET scans on a single subject, as in a test–retest study, it is impossible to determine whether those binding differences were because of interindividual or within-subject variation in humans.

The current test–retest study indicates that the within-subject variation of [^{11}C]ABP688 binding is high. However, the variation is not random.

Table 2 Difference in volume of distribution (V_T) between test and retest for four models

	Two-tissue compartment, constrained			*Two-tissue compartment, non-iterative*			*Logan*			*LEGA*		
	Test V_T *(mL/cc)*	*Retest* V_T *(mL/cc)*	*PD (%)*	*Test* V_T *(mL/cc)*	*Retest* V_T *(mL/cc)*	*PD (%)*	*Test* V_T *(mL/cc)*	*Retest* V_T *(mL/cc)*	*PD (%)*	*Test* V_T *(mL/cc)*	*Retest* V_T *(mL/cc)*	*PD (%)*
Insula	2.42 ± 0.55	2.75 ± 0.56	17 ± 14	2.36 ± 0.58	2.73 ± 0.56	19 ± 14	2.49 ± 0.62	2.81 ± 0.54	19 ± 12	2.57 ± 0.65	2.90 ± 0.55	19 ± 12
Ventral striatum	2.34 ± 0.58	2.65 ± 0.46	17 ± 18	2.29 ± 0.57	2.62 ± 0.42	19 ± 17	2.40 ± 0.62	2.7 ± 0.45	21 ± 14	2.50 ± 0.64	2.79 ± 0.46	21 ± 14
Temporal lobe	2.22 ± 0.58	2.59 ± 0.60	17 ± 17	2.19 ± 0.52	2.56 ± 0.53	16 ± 12	2.27 ± 0.56	2.63 ± 0.57	17 ± 16	2.34 ± 0.58	2.71 ± 0.58	17 ± 16
Cingulate	2.20 ± 0.58	2.51 ± 0.56	16 ± 17	2.10 ± 0.53	2.48 ± 0.54	19 ± 16	2.27 ± 0.56	2.55 ± 0.54	16 ± 15	2.35 ± 0.58	2.64 ± 0.54	17 ± 15
Medial prefrontal cortex	2.24 ± 0.53	2.48 ± 0.57	14 ± 15	2.13 ± 0.49	2.45 ± 0.53	17 ± 12	2.28 ± 0.56	2.54 ± 0.55	18 ± 11	2.35 ± 0.59	2.62 ± 0.56	19 ± 11
Cerebellar gray Matter	1.23 ± 0.28	1.34 ± 0.30	14 ± 11	1.25 ± 0.29	1.35 ± 0.30	12 ± 11	1.34 ± 0.32	1.42 ± 0.33	11 ± 11	1.38 ± 0.33	1.46 ± 0.34	12 ± 11

LEGA, likelihood estimation in graphical analysis; PD, percent difference; V_T, volume of distribution.
The mean and standard deviation of V_T values are shown for all test and retest scans. The five highest binding regions from Table 1, as well as the reference region, are listed.

Instead, average [^{11}C]ABP688 binding increases between scans. This robust test–retest finding is mostly uniform across regions (Table 1) and is significant, based on a linear mixed effects model, regardless of outcome measure used (V_T, BP_P, or BP_{ND}). In addition, V_T and BP_P of most individual regions show significant increases between test and retest in *post hoc* testing, and even BP_{ND} measures, which are not sensitive to tracer concentration in plasma or free fraction measurements, show mostly significant or trend-level increases in binding between scans.

This type of systematic increase in ligand binding between test and retest scans (Figure 3) has not been observed in other test–retest studies conducted in this group using a variety of ligands (and targets), such as [^{11}C]DASB (serotonin transporter), [^{11}C]CUMI (5-HT$_{1A}$ receptor), [^{11}C]McN-5652 (serotonin transporter), [^{11}C]PE2I (dopamine transporter), and [^{11}C]WAY-100635 (5-HT$_{1A}$ receptor) (DeLorenzo *et al*, 2009*b*; Milak *et al*, 2008; Ogden *et al*, 2007; Parsey *et al*, 2000*a*, *b*). Importantly, this increase was also not observed in the [^{11}C]ABP688 baboon test–retest study performed by this group, with the same ligand preparation, scanning technique, and image analysis (DeLorenzo *et al*, 2011). Therefore, the cause of this systematic increase remains an open question. The variables most likely to cause binding differences—injected mass, injected dose, or clearance—did not significantly change between test and retest scans. Low-clearance ICC coupled with the non-significant difference between test and retest clearance rates suggests within-subject variation in clearance that, unlike [^{11}C]ABP688 binding, is not in a single direction (i.e., clearance values do not all increase, Table 3). However, ICC values of the area under the metabolite curve and time to the plasma peak were high, indicating higher variance in these measures between subjects than within a subject. Even if the within-subject variation of plasma activity and metabolism is low, however, as Figure 4 indicates, it is possible to have nearly identical test and retest plasma activity and ligand metabolism, with drastically different TACs.

It should also be noted that [^{11}C]ABP688 variability was not dependent on scan length (data not shown). This is not surprising given the stability of the data, as indicated by the TACs (Figure 2), and based on a simulation study performed by Treyer *et al* (2007), which showed stable V_T values with as little as 20 minutes of scan time.

As the binding increases between scans could not be linked to any of the measured variables (or choice of modeling technique, Table 2), these increases are most likely attributable to a variable that was not measured, such as changes in free fraction or physiological variability. In this work, reliable estimates of BP_F could not be attained because the free fraction was too low to be accurately measured. If the free fraction did vary between test and retest scans, this change could be responsible for the

Table 3 [^{11}C]ABP688-injected mass and clearance for test and retest scans

	Subject 1	*Subject 2*	*Subject 3*	*Subject 4*	*Subject 5*	*Subject 6*	*Subject 7*	*Subject 8*	*Mean*
Test-injected mass (μg)	5.31	5.30	4.98	4.94	0.67	5.57	5.18	2.72	4.33 ± 1.73
Retest-injected mass (μg)	5.60	5.08	5.02	3.73	5.08	4.06	4.96	2.21	4.47 ± 1.09
Test clearance (L/h)	57.1	69.5	74.4	78.8	79.2	74.7	75.9	87.8	74.7 ± 8.8
Retest clearance (L/h)	77.6	58.4	94.4	69.8	93.0	92.5	75.4	88.2	81.2 ± 13.0

The injected mass (μg) and clearance (L/h) are listed for both test and retest scans. There was no significant difference in mass injected ($P = 0.84$) or clearance ($P = 0.20$) between test and retest scans.

detected binding differences. Although this is possible, there is no intuitive reason for free fraction to significantly change in a consistent direction (i.e., to always increase between scans), especially when this effect was not observed in the baboon studies. In addition, it is likely that a change in free fraction would have resulted in a significant difference in reference region V_T (which was not observed), and free fraction changes cannot explain the increases observed in BP_{ND}.

Although there is no reason to believe that binding changes were because of free fraction variation, this cannot be definitively ruled out without estimates of ABP688 free fraction. In this (and our previous baboon) work, the free fraction was determined using an ultrafiltration technique, owing to its short analysis time and lack of dilution effects or volume shifts (Kwon, 2001). However, the accuracy of this technique can suffer because of nonspecific binding of the drug to the plastic tube or ultrafiltration membrane (Kwon, 2001). This problem is exacerbated with highly protein-bound drugs such as ABP688, leading to inconsistent and unreliable results. To avoid this problem in future studies, plasma free fraction can be evaluated using equilibrium dialysis with volume shift correction (Lohman, 1986).

Another possibility that is often explored in connection with ligand binding differences are changes in P-glycoprotein (P-gp). The P-gp can be responsible for ligand efflux through the blood–brain barrier (Doze *et al*, 2000; Ishiwata *et al*, 2007). As such, modulators of P-gp, such as cyclosporine A, can increase the uptake of ligand in the brain (Doze *et al*, 2000; Ishiwata *et al*, 2007). If ABP688 were a substrate for P-gp, the increased binding observed in the retest scans could be because of diminished efflux of ABP688 from the brain. However, there is no evidence indicating that ABP688 is a P-gp substrate. In addition, the tracer doses in which ABP688 is administered are unlikely to cause such systemic effects to the blood–brain barrier, lasting several hours. Therefore, this possibility is also unlikely.

In addition to the above hypotheses, it is also possible that ABP688 binding increases were caused by physiological differences, such as changes in endogenous glutamate occurring in the brain between scans. A recently published pilot study performed in baboons suggests that [^{11}C]ABP688 is sensitive to endogenous glutamate variation (Miyake *et al*, 2011). In this study, *N*-acetylcysteine was used to induce extrasynaptic glutamate release in baboons. *N*-acetylcysteine administration resulted in a decrease in [^{11}C]ABP688 BP_{ND} between baseline and post-*N*-acetylcysteine PET scans. The posited mechanism of action (which remains to be tested) was a shift in affinity of the allosteric binding site for the tracer because of the *N*-acetylcysteine-induced glutamate increase.

Although further testing is required to definitely assess this possibility, if this tracer were sensitive to endogenous glutamate release, as suggested by the baboon pilot study, it may provide insight into the systematic increases observed in this study. It is possible that the stress of the first PET scan, including arterial and venous catheter placement, caused an increase in the levels of glutamate in the brain (Barkus *et al*, 2010; Cortese *et al*, 2010). This increased glutamate may have resulted in lower [^{11}C]ABP688 binding, potentially because of an affinity shift of the receptor for the ligand. During the second scan, subjects were less likely to be anxious, because they were aware of the process and because the arterial and venous lines did not need to be replaced. (Note: The one exception to this is subject 4, who received PET scans on two different days. However, even this subject, having already experienced the process, may have been more relaxed during the second scan.) This may explain the higher binding observed in the retest scan. If this hypothesis is validated, the current study may be the first to report detection of glutamate level variation in humans using [^{11}C]ABP688.

Similar to the use of dopamine antagonist PET tracers to monitor dopamine transmission in disorders such as schizophrenia and substance abuse (Guo *et al*, 2010), if changes in levels of endogenous glutamate affect [^{11}C]ABP688 binding, this ligand could be used to monitor endogenous glutamate level variations in neurological and psychiatric disorders, as well as in response to treatment. This type of assessment may also help tailor treatments to individuals (by monitoring treatment-induced glutamate changes). Although there are numerous potential applications for a tracer that can detect endogenous glutamate variation, without the ability to compensate for this potential intrasubject variability, some conventional PET tracer applications become difficult. For example, typical applications

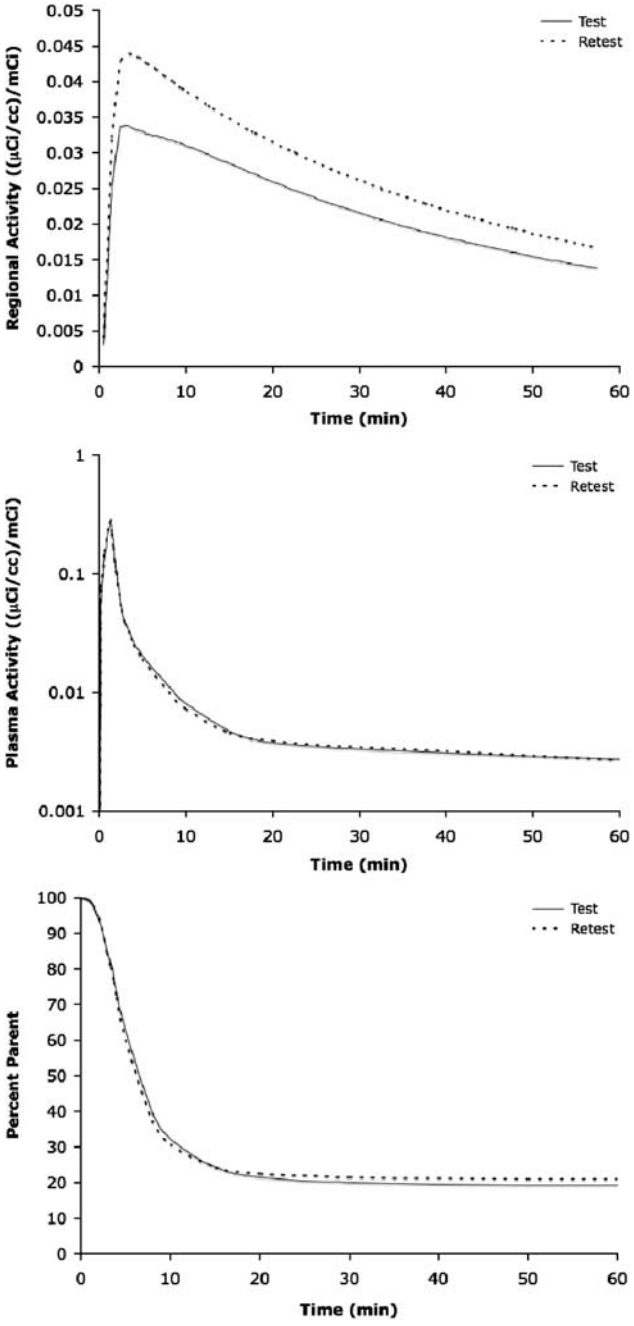

Figure 4 Examination of time–activity curves divided by injected dose (top), plasma concentration divided by injected dose (middle), and percent parent (bottom) of [^{11}C]ABP688 in the ventral striatum of one subject. Time–activity curves were fit with an unconstrained, iterative two-tissue compartment model. The plasma concentration was fit with a straight line and the sum of three exponentials before and after the peak, respectively. The metabolite data were fit with a Hill function. The injected doses for these scans were 15.52 and 14.59 mCi for test and retest, respectively. The clearance values calculated from metabolite-corrected plasma curve were 87.8 and 88.2 L/h for test and retest, respectively.

of this tracer would include occupancy studies for mGluR5 agonists and antagonists, as well as group comparisons of mGluR5 distribution in healthy controls versus patients with psychiatric disorders. For those types of applications, good test–retest reliability and low variability are required; otherwise ligand-binding variability can obscure occupancy effects or group differences. However, as shown in Table 1, the ICCs of [^{11}C]ABP688 outcome measures are low to moderate, meaning that within-subject variation is comparable to the between-subject variation. The significant intrasubject variation observed in the current study, as well as the variability between measurements observed in this and previous studies, regardless of its origins, may signal difficulties in using [^{11}C]ABP688 for these types of applications in humans.

However, it is interesting to note that although [^{11}C]ABP688 binding generally increases between test and retest scans, the binding variability (as indicated by standard deviation) decreases in almost all cases, across all outcome measures (Table 1). Consistent with the endogenous glutamate hypothesis, larger binding variation in the test (compared with retest) scans may be because of differences in the stress response between individuals. Therefore, lower variability in the retest scans may imply that, as the stress subsides, measures of binding become more consistent.

Conclusion

This test–retest study confirms that [^{11}C]ABP688 binds to mGluR5-rich brain regions and that modeling [^{11}C]ABP688 kinetics with an unconstrained 2TC model is appropriate in humans. The test–retest paradigm also allowed assessment of within-subject binding variability in humans, revealing an increase in binding between test and retest scans that was not because of the tracer injected mass, dose, or clearance. This binding variation could make quantification of drug occupancy using [^{11}C]ABP688 difficult.

As this type of increase was not observed in [^{11}C]ABP688 baboon test–retest studies (nor in the numerous human studies performed by our group using several other ligands), it may be because of glutamate level variation in response to the stress of the PET scans. This hypothesis requires further investigation. If this is the case, however, [^{11}C]ABP688 may be able to monitor glutamate level variations in neurological and psychiatric disorders, as well as in response to treatment.

Disclosure/conflict of interest

The authors declare no conflict of interest.

References

Aguirre JA, Kehr J, Yoshitake T, Liu FL, Rivera A, Fernandez-Espinola S, Andbjer B, Leo G, Medhurst AD, Agnati LF, Fuxe K (2005) Protection but maintained

dysfunction of nigral dopaminergic nerve cell bodies and striatal dopaminergic terminals in MPTP-lesioned mice after acute treatment with the mGluR5 antagonist MPEP. *Brain Res* 1033:216–20

Ametamey SM, Kessler LJ, Honer M, Wyss MT, Buck A, Hintermann S, Auberson YP, Gasparini F, Schubiger PA (2006) Radiosynthesis and preclinical evaluation of 11C-ABP688 asa probe for imaging the metabotropic glutamate receptor subtype 5. *J Nucl Med* 47:698–705

Ametamey SM, Treyer V, Streffer J, Wyss MT, Schmidt M, Blagoev M, Hintermann S, Auberson Y, Gasparini F, Fischer UC, Buck A (2007) Human PET studies of metabotropic glutamate receptor subtype 5 with 11C-ABP688. *J Nucl Med* 48:247–52

Ardekani BA, Guckemus S, Bachman A, Hoptman MJ, Wojtaszek M, Nierenberg J (2005) Quantitative comparison of algorithms for inter-subject registration of 3D volumetric brain MRI scans. *J Neurosci Methods* 142:67–76

Avants B, Klein A, Tusttison N, Woo J, Gee J (2010) Evaluation of open-access, automated brain extraction method on multi-site multi-disorder data. In: *16th Annual Meeting for the Organization of Human Brain Mapping*, Barcelona, Spain

Barkus C, McHugh SB, Sprengel R, Seeburg PH, Rawlins JN, Bannerman DM (2010) Hippocampal NMDA receptors and anxiety: at the interface between cognition and emotion. *Eur J Pharmacol* 626:49–56

Cortese BM, Mitchell TR, Galloway MP, Prevost KE, Fang J, Moore GJ, Uhde TW (2010) Region-specific alteration in brain glutamate: possible relationship to risk-taking behavior. *Physiol Behav* 99:445–50

DeLorenzo C, Klein A, Mikhno A, Gray N, Zanderigo F, Mann JJ, Parsey RV (2009*a*) A new method for assessing PET-MRI coregistration. In: *SPIE Medical Imaging*, Bellingham, WA: SPIE; 2009: 72592W-72598

DeLorenzo C, Kumar JS, Zanderigo F, Mann JJ, Parsey RV (2009*b*) Modeling considerations for *in vivo* quantification of the dopamine transporter using [(11)C]PE2I and positron emission tomography. *J Cereb Blood Flow Metab* 29:1332–45

DeLorenzo C, Milak MS, Brennan KG, Kumar JS, Mann JJ, Parsey RV (2011) *In vivo* positron emission tomography imaging with [(11)C]ABP688: binding variability and specificity for the metabotropic glutamate receptor subtype 5 in baboons. *Eur J Nucl Med Mol Imaging* 38:1083–94

Dolen G, Bear MF (2008) Role for metabotropic glutamate receptor 5 (mGluR5) in the pathogenesis of fragile X syndrome. *J Physiol* 586:1503–8

Doze P, Van Waarde A, Elsinga PH, Hendrikse NH, Vaalburg W (2000) Enhanced cerebral uptake of receptor ligands by modulation of P-glycoprotein function in the blood-brain barrier. *Synapse* 36:66–74

Elia J, Gai X, Xie HM, Perin JC, Geiger E, Glessner JT, D'Arcy M, Deberardinis R, Frackelton E, Kim C, Lantieri F, Muganga BM, Wang L, Takeda T, Rappaport EF, Grant SF, Berrettini W, Devoto M, Shaikh TH, Hakonarson H, White PS (2010) Rare structural variants found in attention-deficit hyperactivity disorder are preferentially associated with neurodevelopmental genes. *Mol Psychiatry* 15:637–46

Gass JT, Osborne MP, Watson NL, Brown JL, Olive MF (2009) mGluR5 antagonism attenuates methamphetamine reinforcement and prevents reinstatement of methamphetamine-seeking behavior in rats. *Neuropsychopharmacology* 34:820–33

Guo N, Guo W, Kralikova M, Jiang M, Schieren I, Narendran R, Slifstein M, Abi-Dargham A, Laruelle M, Javitch JA, Rayport S (2010) Impact of D2 receptor internalization on binding affinity of neuroimaging radiotracers. *Neuropsychopharmacology* 35:806–17

Hintermann S, Vranesic I, Allgeier H, Brulisauer A, Hoyer D, Lemaire M, Moenius T, Urwyler S, Whitebread S, Gasparini F, Auberson YP (2007) ABP688, a novel selective and high affinity ligand for the labeling of mGlu5 receptors: identification, *in vitro* pharmacology, pharmacokinetic and biodistribution studies. *Bioorg Med Chem* 15:903–14

Hirvonen J, Johansson J, Teras M, Oikonen V, Lumme V, Virsu P, Roivainen A, Nagren K, Halldin C, Farde L, Hietala J (2008) Measurement of striatal and extrastriatal dopamine transporter binding with high-resolution PET and [11C]PE2I: quantitative modeling and test-retest reproducibility. *J Cereb Blood Flow Metab* 28:1059–69

Holmes CJ, Hoge R, Collins L, Woods R, Toga AW, Evans AC (1998) Enhancement of MR images using registration for signal averaging. *J Comput Assist Tomogr* 22:324–33

Innis RB, Cunningham VJ, Delforge J, Fujita M, Gjedde A, Gunn RN, Holden J, Houle S, Huang SC, Ichise M, Iida H, Ito H, Kimura Y, Koeppe RA, Knudsen GM, Knuuti J, Lammertsma AA, Laruelle M, Logan J, Maguire RP, Mintun MA, Morris ED, Parsey R, Price JC, Slifstein M, Sossi V, Suhara T, Votaw JR, Wong DF, Carson RE (2007) Consensus nomenclature for *in vivo* imaging of reversibly binding radioligands. *J Cereb Blood Flow Metab* 27:1533–9

Ishiwata K, Kawamura K, Yanai K, Hendrikse NH (2007) *In vivo* evaluation of P-glycoprotein modulation of 8 PET radioligands used clinically. *J Nucl Med* 48:81–7

Kendell SF, Krystal JH, Sanacora G (2005) GABA and glutamate systems astherapeutic targets in depression and mood disorders. *Expert Opin Ther Targets* 9:153–68

Klein A, Andersson J, Ardekani BA, Ashburner J, Avants B, Chiang MC, Christensen GE, Collins DL, Gee J, Hellier P, Song JH, Jenkinson M, Lepage C, Rueckert D, Thompson P, Vercauteren T, Woods RP, Mann JJ, Parsey RV (2009) Evaluation of 14 nonlinear deformation algorithms applied to human brain MRI registration. *Neuroimage* 46:786–802

Kwon Y (2001) *Handbook of essential pharmacokinetics, pharmacodynamics, and drug metabolism for industrial scientists*. New York: Kluwer Academic/Plenum Publishers

Lindsley CW, Shipe WD, Wolkenberg SE, Theberge CR, Williams Jr DL, Sur C, Kinney GG (2006) Progress towards validating the NMDA receptor hypofunction hypothesis of schizophrenia. *Curr Top Med Chem* 6: 771–85

Liu F, Grauer S, Kelley C, Navarra R, Graf R, Zhang G, Atkinson PJ, Popiolek M, Wantuch C, Khawaja X, Smith D, Olsen M, Kouranova E, Lai M, Pruthi F, Pulicicchio C, Day M, Gilbert A, Pausch MH, Brandon NJ, Beyer CE, Comery TA, Logue S, Rosenzweig-Lipson S, Marquis KL (2008) ADX47273 [S-(4-fluoro-phenyl)-\{3-[3-(4-fluoro-phenyl)-[1,2,4]-oxadiazol-5-yl]-piper idin-1-yl\}-methano. *J Pharmacol Exp Ther* 327:827–39

Logan J, Fowler JS, Volkow ND, Wolf AP, Dewey SL, Schlyer DJ, MacGregor RR, Hitzemann R, Bendriem B, Gatley SJ, Christman DR (1990) Graphical analysis of reversible radioligand binding from time-activity measurements applied to [N-11C-methyl]-(-)-cocaine PET studies in human subjects. *J Cereb Blood Flow Metab* 10:740–7

Logan J, Fowler JS, Volkow ND, Wang GJ, Ding YS, Alexoff DL (1996) Distribution volume ratios without blood sampling from graphical analysis of PET data. *J Cereb Blood Flow Metab* 16:834–40

Lohman JJHM (1986) Plasma-protein binding of drugs—implications for therapeutic drug-monitoring. *Pharm Weekblad-Sci Ed* 8:302–4

Markou A (2009) Accruing preclinical evidence aboutmetabotropic glutamate 5 receptor antagonists as treatments for drug dependence highlights the irreplaceable contributions of animal studies to the discovery of new medications for human disorders. *Neuropsychopharmacology* 34:817–9

Milak MS, Severance AJ, Ogden RT, Prabhakaran J, Kumar JS, Majo VJ, Mann JJ, Parsey RV (2008) Modeling considerations for 11C-CUMI-101, an agonist radiotracer for imaging serotonin 1A receptor *in vivo* with PET. *J Nucl Med* 49:587–96

Miyake N, Skinbjerg M, Easwaramoorthy B, Kumar D, Girgis RR, Xu X, Slifstein M, Abi-Dargham A (2011) Imaging changes in glutamate transmission *in vivo* with the metabotropic glutamate receptor 5 tracer [(11)C] ABP688 and N-acetylcysteine challenge. *Biol Psychiatry* 69:822–4

Ogden RT (2003) Estimation of kinetic parameters in graphical analysis of PET imaging data. *Stat Med* 22:3557–68

Ogden RT, Ojha A, Erlandsson K, Oquendo MA, Mann JJ, Parsey RV (2007) *In vivo* quantification of serotonin transporters using [(11)C]DASB and positron emission tomography in humans: modeling considerations. *J Cereb Blood Flow Metab* 27:205–17

Palucha A, Pilc A (2007) Metabotropic glutamate receptor ligands aspossible anxiolytic and antidepressant drugs. *Pharmacol Ther* 115:116–47

Parsey RV, Kegeles LS, Hwang DR, Simpson N, Abi-Dargham A, Mawlawi O, Slifstein M, Van Heertum RL, Mann JJ, Laruelle M (2000*a*) *In vivo* quantification of brain serotonin transporters in humans using [11C]McN 5652. *J Nucl Med* 41:1465–77

Parsey RV, Slifstein M, Hwang DR, Abi-Dargham A, Simpson N, Mawlawi O, Guo NN, Van Heertum R, Mann JJ, Laruelle M (2000*b*) Validation and reproducibility of measurement of 5-HT1A receptor parameters with [carbonyl-11C]WAY-100635 in humans: comparison of arterial and reference tissue input functions. *J Cereb Blood Flow Metab* 20:1111–33

Pilc A, Chaki S, Nowak G, Witkin JM (2008) Mood disorders: regulation by metabotropic glutamate receptors. *Biochem Pharmacol* 75:997–1006

Shrout PE, Fleiss JL (1979) Intraclass correlations: uses in assessing rater reliability. *Psychol Bull* 86:420–8

Siegel GJ (2006) *Basic Neurochemistry: Molecular, Cellular, and Medical Aspects* 7th ed. Amsterdam; Boston, MA: Elsevier

Spooren W, Ballard T, Gasparini F, Amalric M, Mutel V, Schreiber R (2003) Insight into the function of Group I and Group II metabotropic glutamate (mGlu) receptors: behavioural characterization and implications for the treatment of CNS disorders. *Behav Pharmacol* 14:257–77

Treyer V, Streffer J, Wyss MT, Bettio A, Ametamey SM, Fischer U, Schmidt M, Gasparini F, Hock C, Buck A (2007) Evaluation of the metabotropic glutamate receptor subtype 5 using PET and 11C-ABP688: assessment of methods. *J Nucl Med* 48:1207–15

Turle-Lorenzo N, Breysse N, Baunez C, Amalric M (2005) Functional interaction between mGlu 5 and NMDA receptors in a rat model of Parkinson's disease. *Psychopharmacology (Berl)* 179:117–27

Wu S, Ogden RT, Mann JJ, Parsey RV (2007) Optimal metabolite curve fitting for kinetic modeling of 11C-WAY-100635. *J Nucl Med* 48:926–31

Wyss MT, Ametamey SM, Treyer V, Bettio A, Blagoev M, Kessler LJ, Burger C, Weber B, Schmidt M, Gasparini F, Buck A (2007) Quantitative evaluation of 11C-ABP688 asPET ligand for the measurement of the metabotropic glutamate receptor subtype 5 using autoradiographic studies and a beta-scintillator. *Neuroimage* 35: 1086–92